

Airborne Ocean Surveys of the Loop Current Complex From NOAA WP-3D in Support of the *Deepwater Horizon* Oil Spill

Lynn K. Shay,¹ Benjamin Jaimes,¹ Jodi K. Brewster,¹ Patrick Meyers,¹ E. Claire McCaskill,¹ Eric Uhlhorn,² Frank Marks,² George R. Halliwell Jr.,³ Ole Martin Smedstad,⁴ and Patrick Hogan⁵

At the time of the *Deepwater Horizon* oil rig explosion, the Loop Current (LC), a warm ocean current in the Gulf of Mexico (GoM), extended to 27.5°N just south of the rig. To measure the regional scale variability of the LC, oceanographic missions were flown on a NOAA WP-3D research aircraft to obtain ocean structural data during the spill and provide thermal structure profiles to ocean forecasters aiding in the oil spill disaster at 7 to 10 day intervals. The aircraft flew nine grid patterns over the eastern GoM between May and July 2010 deploying profilers to measure atmospheric and oceanic properties such as wind, humidity, temperature, salinity, and current. Ocean current profilers sampled as deep as 1500 m, conductivity, temperature, and depth profilers sampled to 1000 m, and bathythermographs sampled to either 350 or 800 m providing deep structural measurements. Profiler data were provided to modeling centers to predict possible trajectories of the oil and vector ships to regions of anomalous signals. In hindcast mode, assimilation of temperature profiles into the Hybrid Coordinate Ocean Model improved the fidelity of the simulations by reducing RMS errors by as much as 30% and decreasing model biases by half relative to the simulated thermal structure from models that assimilated only satellite data. The synoptic snapshots also provided insight into the evolving LC variability, captured the shedding of the warm core eddy Franklin, and measured the small-scale cyclones along the LC periphery.

1. INTRODUCTION

¹Rosenstiel School of Marine and Atmospheric Science, Division of Meteorology and Physical Oceanography, University of Miami, Miami, Florida, USA.

²NOAA Atlantic Oceanographic and Meteorological Laboratory, Hurricane Research Division, Miami, Florida, USA.

³NOAA Atlantic Oceanographic and Meteorological Laboratory, Physical Oceanography Division, Miami, Florida, USA.

⁴QinetiQ North America, Stennis Space Center, Mississippi, USA.

⁵Naval Research Laboratory, Stennis Space Center, Mississippi, USA.

Monitoring and Modeling the *Deepwater Horizon* Oil Spill:
A Record-Breaking Enterprise
Geophysical Monograph Series 195
Copyright 2011 by the American Geophysical Union.
10.1029/2011GM001101

On 20 April 2010, the *Deepwater Horizon* (DwH) oil rig, located at a water depth of ~1675 m on the northern continental slope of the Gulf of Mexico (GoM) adjacent to the DeSoto Canyon, exploded causing a major oil spill that lasted for 107 days until it was capped on 15 July. At the time of the explosion, the Loop Current (LC) extended north of its mean position where the average maximum northward extension of the LC intrusion is 26.2°N [*Leben*, 2005; *Vukovich*, 2007]. The northern edge of the LC extended to ~27.5° N during the first few weeks of the oil spill based on the sea surface height field where surface geostrophic velocities exceeded 1.5 m s⁻¹.

The anticyclonically rotating LC generally has two forms: a retraction phase where the LC makes a direct link from the Yucatan Straits to the Florida Straits as observed during 2002

[Shay and Uhlhorn, 2008], and a bulging phase, where the LC meanders deep into the GoM before exiting to the east through the Florida Straits [Nof, 2005]. Surrounding a bulging LC is a complex eddy field including both cyclonic and anticyclonically rotating eddies [Schmitz, 2005; Vukovich, 2007]. The larger anticyclonically rotating warm core eddies (WCE) have a vertical scale of $O(1000\text{ m})$ with diameters between 200 and 400 km [Mooers and Maul, 1998]. By contrast, smaller-scale cyclonically rotating cold core eddies (CCE) are found along the periphery of the LC [Hamilton, 1992; Zavala-Hidalgo et al., 2003] and are vitally important in the shedding of the WCEs from the LC through current instabilities [Schmitz, 2005; Chérubin et al., 2005]. That is, the LC bulge eventually may pinch off and form a WCE, which moves to the west to southwest at speeds of a few km d^{-1} [Elliot, 1982; Sturges and Leben, 2000]. Because the LC path was characteristic of this bulging phase during the spill similar to that observed during Hurricanes Katrina and Rita [Scharroo et al., 2005; Jaimes and Shay, 2009], a possibility existed for oil to be transported from the northern GoM to the southern tip of Florida and into the Florida Current and Gulf Stream, potentially impacting the ecosystems of the Florida Keys and the southeast coast of Florida.

During the summer of 2010, the bulging LC intrusion was followed by a series of attachments and reattachments of WCE Franklin that influenced the ocean current structure south of the rig [Hamilton et al., this volume; Walker et al., this volume]. As shown in Figure 1, smaller-scale cyclonic eddies were located along the northern extent of the LC that impacted the circulation patterns near the rig during most of the observational period and facilitated the entrainment of oil into the LC [Walker et al., this volume; Liu et al., this volume].

In this broader context, emergency responders and modeling teams were concerned the LC and its complex eddy field would be a major mechanism for oil transport throughout the GoM. In addition to satellite measurements for the surface layer, near real-time information on LC properties using various in situ platforms was needed to monitor its position and subsurface ocean structure because this spill was subsurface. A NOAA research aircraft flew oceanographic

survey missions to provide synoptic oceanic and atmospheric measurements to provide guidance to the ocean forecast community and emergency responders on the LC variability. These flights provided near real-time temperature profile data over 7 to 10 days intervals for assimilation into ocean models at forecasting centers such as the Naval Oceanographic Office to predict the circulation and potential pathways of the oil. These measurements provided data to vector ships such as the NOAA R/V *Nancy Foster* to regions of mesoscale variability and were used to evaluate satellite-based products such as oceanic heat content [Mainelli et al., 2008]. In this manuscript, the oceanographic surveys are described in section 2 including a brief description of the sensor packages and their respective measurement uncertainties. Section 3 discusses the observed variability from the oceanic and atmospheric profilers and salient results such as the subsurface thermostad observed in the northwestern part of the grid as well as comparisons to satellite-derived isotherm depths (20°C isotherm depth: H_{20}) from altimetry. Section 4 focuses on twin assimilation experiments that ingest and deny the thermal structure data from the oceanographic surveys into the Hybrid Coordinate Ocean Model (HYCOM). The results are summarized in section 5 with concluding remarks with an emphasis on future research efforts.

2. AIRBORNE OCEAN SURVEYS

Nine flights on NOAA's WP-3D Orion aircraft were conducted between 8 May and 9 July 2010 (Figure 1) over the region extending from just south of the DwH rig southward over the LC and associated frontal eddies. Expendable probes measured atmospheric and oceanic properties every 7 to 10 days over the northeastern GoM. In total, 588 airborne profilers were deployed (Table 1), specifically 405 bathythermographs (airborne expendable bathythermographs (AXBTT)), 142 current-temperature profilers (airborne expendable current profiler (AXCP)), and 41 conductivity-temperature-depth profilers (airborne expendable conductivity temperature and depth profiler (AXCTD)). The configuration of the aircraft sampling pattern was similar to that used during NOAA's

Figure 1. (opposite) Eight of the nine flight tracks of the WP-3D and profiler drop points overlaid on absolute sea surface height (SSH, color) and altimetry-derived geostrophic currents (arrows). Yellow triangles are for the position of the DwH rig; red and white circles are for good and bad profilers, respectively. The absolute SSH (or η) and surface geostrophic currents were derived from: Daily maps from satellite-based measurements of the surface height anomaly (SHA) from NASA Jason-1 and Jason-2, and European Space Agency (ESA) Envisat from May to July 2010; η was estimated for the entire GoM by adding the SHA fields to the Combined Mean Dynamic Topography Rio05 [Rio and Hernandez, 2004], representing the mean sea surface height above a geoid computed over a 7 year period (1993–1999); and surface geostrophic flows ($\mathbf{V}_g = U_g\mathbf{i} + V_g\mathbf{j}$) from the horizontal gradients in η ($U_g = -(g/f)\partial\eta/\partial y$, $V_g = (g/f)\partial\eta/\partial x$, where f is the Coriolis parameter). Note the maximum surface current vector is 2 m s^{-1} . Dark blue and red shades of SSH are for cyclonic and anticyclonic geostrophic features, respectively.

Hurricane Intensity Forecast Experiments [Rogers *et al.*, 2006]. During the first seven flights, failure rates for the AXCPs were unusually high compared to other experiments. These hardware problems included radio frequency (RF) transmission where either the transmitters did not turn on

(e.g., no RF quieting) or the RF signals were too low to be detected. These problems were resolved during the final missions where the failure rate was less than 10%. Despite these problems with the AXCPs, the thermal structure over the LC system was well resolved from the aircraft measurements.

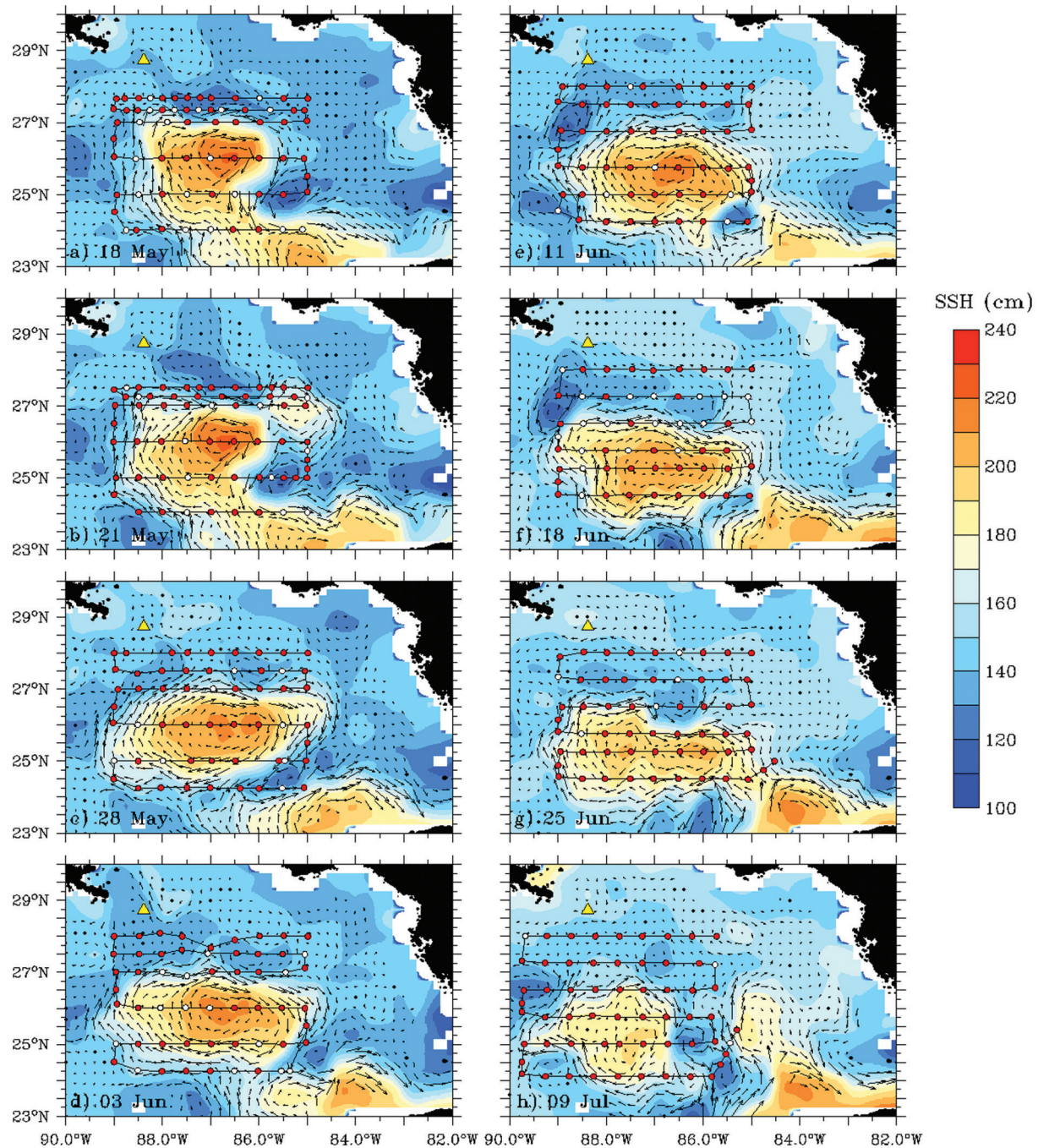


Figure 1

Table 1. Number and Type of Expendable Profilers Deployed During the DwH Oil Spill^a

Flight Number	Date	Air-Dropped (or Aircraft-Deployed or Airborne Expendable Bathythermograph)	AXCTD	AXCP	Total
100508H	08 May	52 (46)	0	0	52 (46)
100518H	18 May	29 (28)	11 (10)	26 (10)	66 (48)
100521H	21 May	42 (41)	2 (2)	22 (11)	66 (54)
100528H	28 May	41 (37)	2 (1)	22 (12)	65 (50)
100603H	03/04 Jun	37 (33)	6 (6)	23 (9)	66 (48)
100611H	11 Jun	53 (48)	0	15 (10)	68 (58)
100618H	18 Jun	34 (23)	8 (7)	22 (11)	64 (41)
100625H	25 Jun	58 (53)	6 (6)	0	64 (59)
100709H	09 Jul	59 (54)	6 (3)	12 (11)	77 (68)
Total		405 (363)	41 (35)	142 (74)	588 (472)

^aFirst number in column is total number deployed; second number in parentheses is total successful profiles.

2.1. Flight Tracks

Research flights on the NOAA aircraft departed from MacDill Air Force Base and had durations of 8 to 10 h. During a typical mission, the aircraft flew at ~1700 m at an indicated air speed between 90 and 95 m s⁻¹ for optimal deployment of the expendable probes. Ocean profilers were deployed in lawnmower style grids (see Figure 1). These flights sampled essentially the same grid points, to as deep as 1500 m, to provide the evolving oceanic variability of the LC associated with the potential shedding of Eddy Franklin. Atmospheric dropsondes [Hock and Franklin, 1999] were deployed in the center of the flight tracks with others deployed along the edges of the LC over the strong frontal zones. On several flights, AXCPs and AXCTDs were deployed at the same points as AXBTs to compare T(z) profiles over the upper 350 m.

During the first two legs of the 8 May 2010 flight (not shown), the aircraft was flown at 350 m to be below the cloud deck and avoid deploying profilers on other aircraft or containment vessels. Five legs of the grid were spaced at 0.5° intervals (~55 km) from 28.4°N to 26.5°N spanning 89°W to 84.5°W. On the sixth drop (86.5°W, 28.3°N), oil globs appeared and then organized into a slick as the aircraft flew westward toward the DwH Site. During the remaining legs of the grid, the flight level was 1700 m. Oil was not seen again until the final leg of our grid where the aircraft traveled due north along 88°W into the main oil spill area. The northern edge of the grid was limited to 28.3°N due to the restricted no-fly zone surrounding the DwH spill.

After the initial flight, the grid was expanded southward to encompass more of the eastern GoM and capture the oceanic variability in the frontal CCEs, which facilitate WCE shedding through baroclinic and barotropic instability (e.g., vertical and horizontal current shear, respectively). More oil slicks were observed in the CCE located at 25°N 85.5°W, and a rainbow oil sheen was observed at 24°N, 85°W as well

as along the northwestern part of the two northernmost legs (Figure 1a). Prior to flying over the final transect, the aircraft dropped to ~1000 m and proceeded northeastward to fly over the well site to calibrate the Stepped Frequency Microwave Radiometer (SFMR) [Uhlhorn *et al.*, 2007] and the downward-looking infrared radiometer thermometer by acquiring data on sea surface properties such as sea surface temperatures (SST) and brightness temperatures. The aircraft flew over brown oil, rainbow and dull sheens, as well as the silver sheens where wind rows of red/orange emulsion surrounded the site as reported in the U.S. Coast Guard (USCG) HC-144 images.

Flight tracks for 18, 21, and 28 May 2010 were similar (Figures 1a–1c) with four transects spaced at 1° intervals in latitude (~110 km) between 24°N and 27°N spanning longitudes from 89°W to 85°W at 0.5° resolution. Along the last two transects at 27°N and 27.5°N, expendable profilers were deployed at 0.25° resolution in the area located due south of the no-fly zone that was sampled during the 8 May flight. On 21 May 2010, additional higher resolution measurements (0.25°) were acquired through the CCE at 25°N, 85.5°W. Along the last two legs from 27°N to 27.5°N, expendable profilers were once again deployed at 0.25° resolution in the area located due south of the no-fly zone sampled during the 8 May flight. Based on analyses from the 28 May SFMR flight data over the oil slick, the brightness temperatures did not change across the thick oil slick and the sheen. This is good news for future hurricane flights because surface winds can be mapped during strong winds even when oil slicks are present.

Flights on 3 and 4 June 2010 (combined as 1 day in Figure 1d) deviated slightly from the typical flight plan. As on the 28 May flight, four of the six legs of the grid were spaced at 1° intervals in latitude (~110 km) from 24.5°N to 27°N and spanning 89°W to 85°W with profiler deployments at 0.5° resolution. The last two transects were at 27.5°N and 28°N with similar spatial resolution. All but one leg of the grid was

finished on 3 June 2010 as the NOAA aircraft landed in Baton Rouge that evening. On the morning of 4 June, the NOAA Administrator (Dr Jane Lubchenco) boarded the aircraft for an aerial view of the spill site, while the aircraft acquired radiometer data and deployed profilers along the northern transect (28°N) of the grid. The aircraft returned to Pascagoula, MS to refuel and for passengers to disembark from the aircraft. The aircraft returned to the northern transect, deployed six profilers, then returned to MacDill Air Force Base.

On 11 June 2010 (Figure 1e), transects were shifted about 0.25° southward from the 3–4 June flights; i.e., from 27°N and 26°N to 26.75°N and 25.75°N. Four of the six legs in the grid were spaced at 1° intervals in latitude (~110 km) from 24.5°N to 27°N spanning 89°W to 85°W with profilers deployed at 0.5° resolution. The last two transects were at 27.5°N and 28°N with similar along-track resolution. Flight tracks from 18, 25 June and 9 July 2010 (Figures 1f–1h) were similar to the 11 June flight.

2.2. Data Acquisition

The aircraft flew at indicated airspeeds (IASs) of 90 to 95 m s⁻¹ to minimize the amount of acceleration that the pro-

filers (particularly AXCPs and AXCTDs) experience during each deployment. As the oceanic profilers are jettisoned from the aircraft, a parachute deploys from the airborne canister. At altitudes of 1500–2000 m, profilers require approximately a minute to arrive at the ocean's surface. Once in the seawater, a battery is activated that turns on a RF transmitter with a small antenna to transmit data to the aircraft over channels 12 (170 MHz), 14 (171.5 MHz), and 16 (173 MHz). After an elapsed time of 20 to 30 s, the probe is released from the airborne canister and starts its descent while remaining attached to the surface unit through a thin gauge wire. Data are multiplexed and sent to the surface unit through this wire and then transmitted to the aircraft. During the period of active sampling (typically 6 to 8 min for the differing profilers), the aircraft traverses about 35 to 40 km down range as AXCPs and AXCTDs descend to 1000 to 1500 m compared to 350 to 800 m depths for shallow and deep AXBTs, respectively.

The AXCP (or expendable current profiler (XCP)) operates on the principle of motional induction as a result of seawater moving through the earth's magnetic field [Sanford *et al.*, 1982]. The electromagnetic force (EMF) induced by the current velocity at a given depth will be relative to the velocities of the surrounding water. Thus, the XCP measures a velocity (and shear) relative to an unknown, depth-independent current.

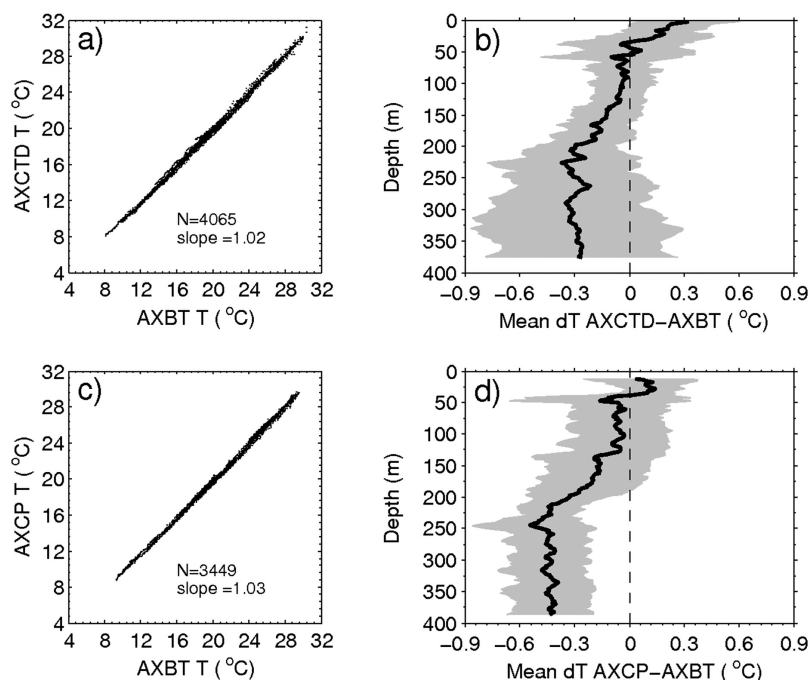


Figure 2. Comparison of temperature (°C) profiles from all WP-3D flights. (a, b) Air-dropped (or aircraft-deployed or airborne expendable bathythermographs (AXBTs) versus AXCTDs (22 sets). (c, d) AXBTs versus AXCPs (20 sets). (b, d) dT represents temperature difference, and the bold line and gray shadow represents the mean and standard deviation of this temperature difference, respectively.

Recent studies have demonstrated that the current profilers are effective in resolving the low-frequency geostrophic and near-inertial flows as well as internal waves [Kunze, 1985; Shay *et al.*, 1998]. Profilers descend at a rate of 4.5 m s^{-1} and accu-

rately sample the vertical structure of these currents at 0.3 m intervals starting at 2 to 4 m beneath the surface in nonhurricane deployments [Shay and Brewster, 2010] and about 10 to 15 m in hurricane deployments [Sanford *et al.*, 1987; Shay *et al.*, 1998].

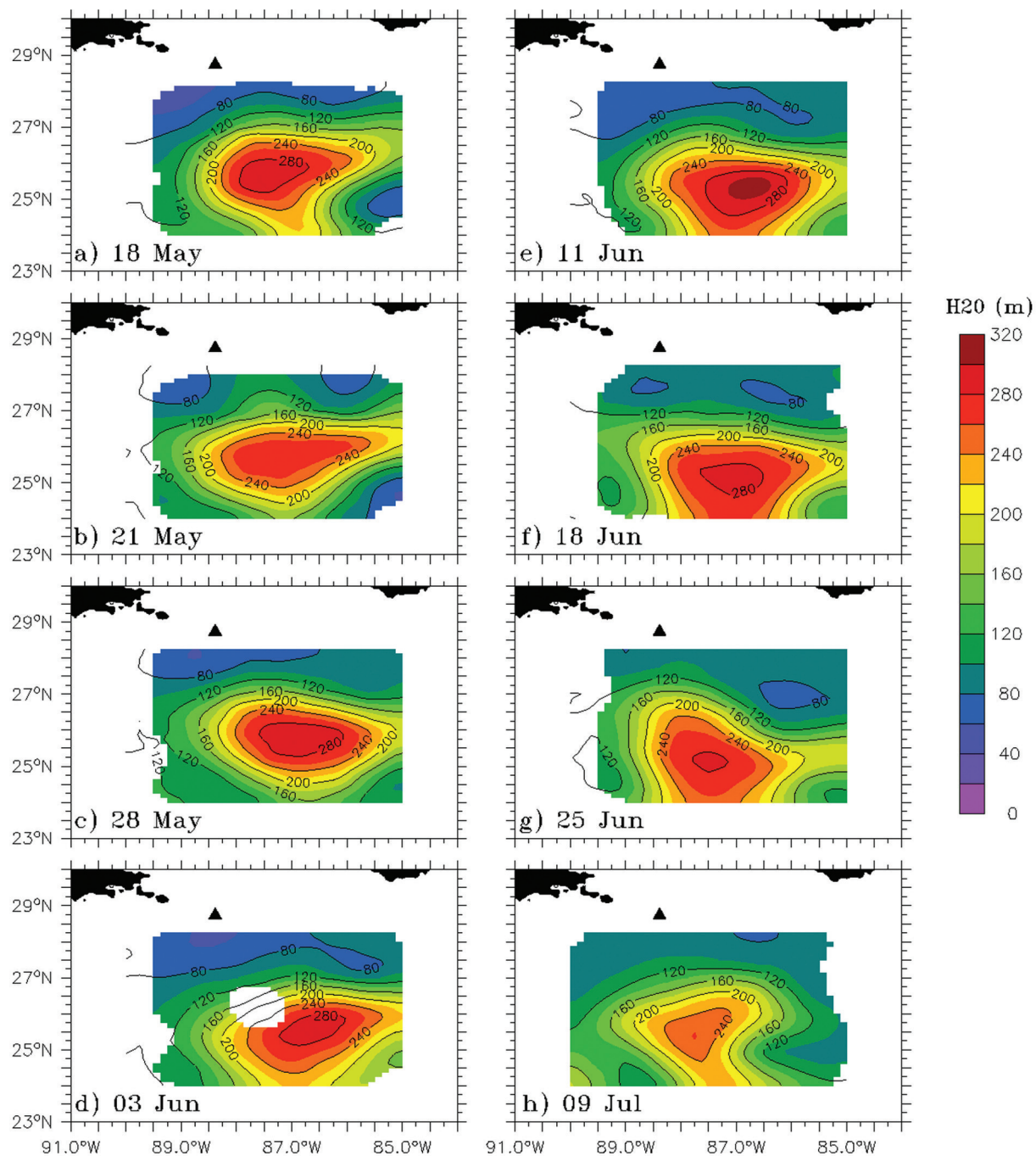


Figure 3. Snapshots of objectively analyzed depth of the 20°C isotherm (H_{20} ; m) from airborne profilers (eight of the nine flights). Blanked regions are points where the mapping error is larger than 60%.

RMS velocity errors range between 1 and 3 cm s^{-1} over 3 m intervals. These velocity errors are well below upper ocean current signals of more than 1 m s^{-1} in the LC domain.

The AXCTD measures conductivity with an inductive cell that detects an EMF in a toroid due to salinity, whereas the temperature is measured by resistance changes in a thermistor. The cited descent rate of the AXCTD is 2.2 m s^{-1} , which is slower than that of the AXCP (4.5 m s^{-1}) but faster than that of the AXBT (1.5 m s^{-1}). The depth accuracy is 2% with a resolution of 11 cm. Upper ocean conductivity (salinity) structure was mapped using AXCTDs within cited accuracies of about 0.03 mS cm^{-1} or 0.05 practical salinity units (psu) and a resolution of 0.015 mS cm^{-1} (0.03 psu) to 1000 m with

depth resolution of 1 m. The temperature accuracy is 0.02°C with a resolution of 0.01°C. Given an accuracy of 0.05 psu in salinity, the corresponding temperature accuracy is 0.12°C in temperature-salinity space, which was within the resolving capability of the AXCTD thermistors. During the Eastern Pacific Investigation of Climate (EPIC) experiment [Raymond *et al.*, 2004], regression analyses between shipboard and aircraft CTD measurements revealed a mean temperature difference of 0.2°C and 0.05 psu [Shay and Brewster, 2010]. Thus, the accuracy and resolution of the AXCTDs is sufficient to determine the salinity structure and resolve the differing water masses between the LC and Gulf Common Water (GCW) [Nowlin and Hubertz, 1972; Jaimes and Shay, 2009].

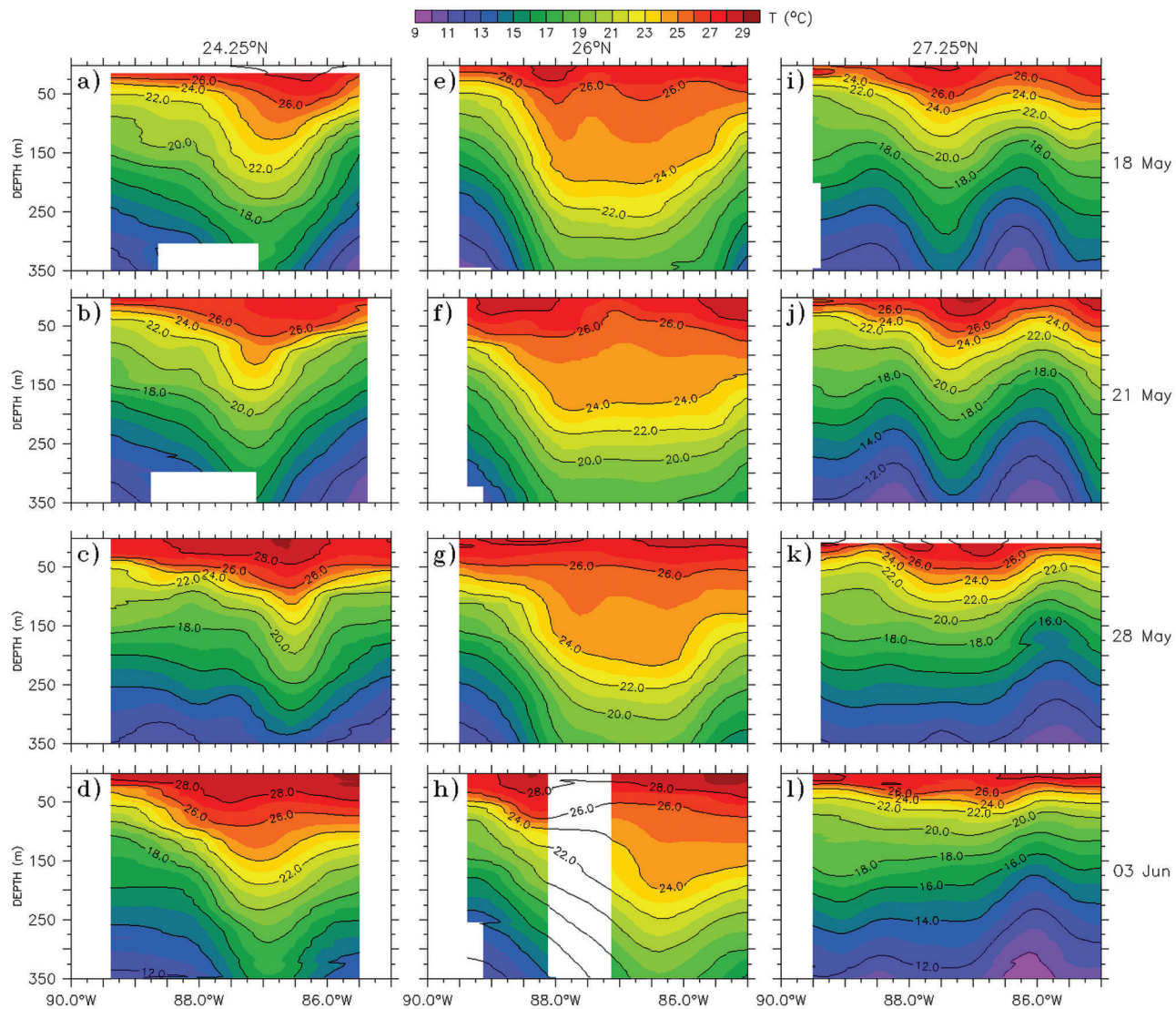


Figure 4. Objectively analyzed vertical sections of temperature ($^{\circ}\text{C}$) from airborne profilers at (a–d) 24.25°N, (e–h) 26°N, and (i–l) 27.25°N. Blanked regions are points where the mapping error is larger than 60%.

2.3. Data Quality Control

All data were stored on digital analog tapes or flash cards for subsequent playback and detailed processing and analyses in the lab. Each temperature profile was compared with surrounding profiles to check for consistency in structure such as mixed layer temperature and depth. Temperature profiles from all profilers were smoothed to form 2 m profiles. Note that temperatures from AXCTDs and AXCPs were compared against temperatures from AXBTs for all points where simultaneous AXCTD/AXBT and AXCP/AXBT profiles were available (22 and 20 points, respectively, Figure 1). Despite differing fall rates, thermal structures measured at the same point by different probes are consistent. Point-by-point comparison of these temperature combinations produced regression slopes of 1.02 and 1.03 (Figures 2a, 2c). The overall RMS temperature differences in the upper 350 m were $\sim 0.4^\circ\text{C}$ for these combinations. A large fraction of the temperature differences was below the 200 m depth level (Figures 2b, 2d). Note that the accuracy of the thermistor is $\pm 0.1^\circ\text{C}$ for AXCTDs [Johnson, 1995], and $\pm 0.2^\circ\text{C}$ for AXBTs and AXCPs [Boyd, 1987], or about one half of the RMS temperature differences obtained from the intercomparisons. Temperature differences in these various combinations increased with depth due to the slower descending profilers (AXBTs) decelerate with depth [Johnson,

1995] where depth errors range from 2% to 5%, while deeper AXBTs have depth errors of about 2% to 3%. This differential depth error explains the temperature difference between probes at depth.

3. OBSERVED OCEANIC VARIABILITY

3.1. Fluctuations of the 20°C Isotherm Depth

During the growing and shedding of WCE Franklin, the LC bulge experienced a series of stretching and straining events represented by fluctuations of the depth of the 20°C isotherm (H_{20} , Figure 3). Maximum values of H_{20} exceeding 250 m were measured on 21 May at the LC bulge, just before the first separation of Franklin. A series of frontal CCEs simultaneously developed along Franklin's periphery, where H_{20} levels were ~ 80 m (Figure 3b). Maximum values of H_{20} exceeding 240 m were observed during the second separation of Franklin on 9 July (Figure 3h). Smaller values of H_{20} in Figures 3b and 3h indicate reduction of available potential energy over the LC bulge, suggestive of baroclinic instability which may play an important role during the WCE shedding events. Numerical studies indicate that the bottom-intensified instability of the LC bulge produce the growth of cyclones in deep layers in the vicinity of the Yucatan Straits [Chérubin *et al.*, 2006]. These smaller-scale cyclones contribute to the separation of the LC

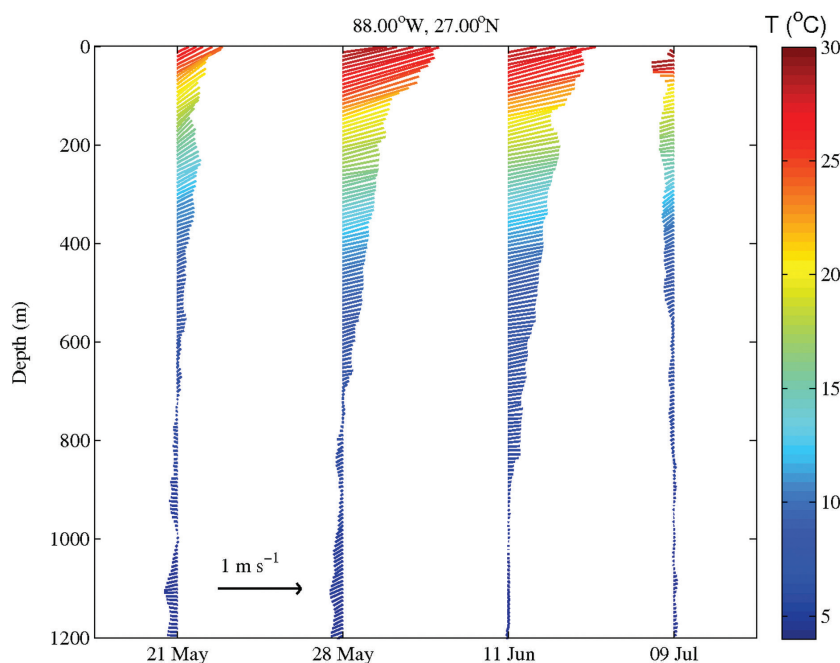


Figure 5. Evolution of horizontal currents at a point located on the northern edge of the Loop Current (LC) ($\sim 88.0^\circ\text{W}$, $\sim 27.0^\circ\text{N}$). (right) Positive values for the velocity components u and v are to the east (top) and to the north, respectively.

bulge (or WCE) from the LC [Schmitz, 2005; Chérubin *et al.*, 2005]. Note that the reduction of H_{20} in Figures 3b and 3h coincides with the intensification of the cyclonic circulation centered at about 25°N and 85.75°W in Figures 1b and 1h, which is in agreement with previous results.

3.2. Thermal Sections

Another view of the separation of Franklin is depicted in Figure 4. The vertical section along the shedding region

(24.25°N) shows deep warm thermal structures and slanting isotherms when Franklin was attached to the LC (Figures 4a, 4b, and 4d). By contrast, these warm thermal structures were shallower, and the isotherms were flattened by 28 May, after Franklin separated from the LC (Figure 4c). Before the shedding event, vertical and horizontal thermal gradients tightened along the east and west flanks of the LC bulge along 26°N transect, presumably by the effect of the strong frontal CCEs (Figures 4e, 4f). These gradients relaxed after the shedding of Franklin (Figure 4g). Frontal CCEs

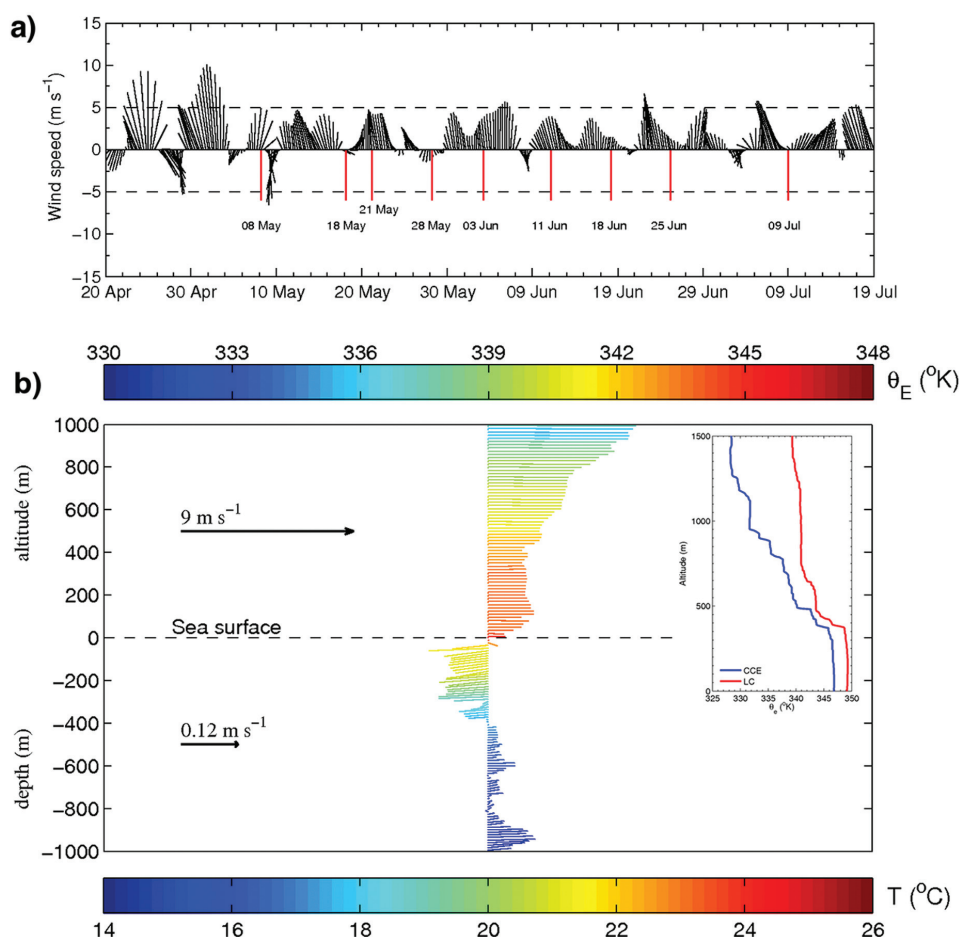


Figure 6. (a) Surface winds (m s^{-1}) at buoy 42040 (29.212°N , 88.207°W or about 55 km to the NE of the DwH rig); this buoy is owned and maintained by National Data Buoy Center. Surface winds are measured at 10 m above site elevation, and original wind speed and direction are averaged over an 8-min period (<http://www.ndbc.noaa.gov>). Here, these surface winds were averaged every 6 h from original 8-min averages. To be consistent with ocean currents, the wind-to-convention is used. Vertical red lines indicate days of WP-3D flights. (b) Vertical distribution of winds (from GPS dropsonde) and ocean currents (from AXCP) at 27.67°N , 88.78°W (Gulf Common Water) from the 18 May WP-3D flight. Upper and lower color scales are for atmospheric equivalent potential temperature (θ_E) and seawater temperature (T), respectively. Positive wind and current components are to the (top) north and (right) east. For comparative purpose, vertical distributions of θ_E over a cold core eddy (CCE) and the LC bulge (from the 18 and 21 May WP-3D flights, respectively) are presented in the inset in (b).

were observed along the 27.25°N transect where the slopes of isotherms were steeper prior to Franklin's separation (Figures 4i, 4j). Thermal gradients were again weaker during the time period that Franklin was separated from the LC (Figure 4k).

3.3. Currents Near the DwH Rig

The intrusion of the LC and the development of northern frontal CCEs impacted the magnitude and direction of horizontal currents near the DwH rig and hence potential pathways of the oil [Walker *et al.*, this volume; Liu *et al.*, this volume]. For example, from 21 May to 11 June, the LC intrusion forced northeast currents at 88°W and 27°N that were surface intensified in the upper 800 m (Figure 5). By contrast, on 9 July, these currents changed direction to the east by the presence of a weaker and colder counterclockwise circulation. Baroclinic current structures were observed from 21 May to 11 June, where currents above the 800 m depth level were directed toward to the northeast, and currents below this depth level were toward the southwest. Intense baroclinic processes have been observed in numerical model simulations during the growing of midlevel and bottom counter-clockwise circulations that may play an essential role in WCE shedding events.

3.4. Wind Fields

During most of the time period of study, the surface winds (from National Data Buoy Center buoy 42040) near the DwH rig were to the north and north-northwest, with speeds of less than 5 m s^{-1} . Only during two isolated events in late April and early May, surface winds to the north-northwest were between 5 and 10 m s^{-1} (Figure 6a). Compared with background ocean currents, these weak surface winds had a minimal impact on the surface horizontal ocean circulations. For example, on 18 May, surface winds to the southeast of less than 3 m s^{-1} produced a weak Ekman-like surface current of less than 0.05 m s^{-1} (Figure 6b). Below the ocean's thin frictional layer, background currents were in the opposite direction to the wind with speeds of $\sim 0.1 \text{ m s}^{-1}$ in the upper ocean (e.g., 300 m).

The equivalent potential temperature (θ_e) is an important state variable in the atmosphere defined as the temperature of an air parcel that ascends psuedo-adiabatically until all its water vapor has been condensed out and then descends dry adiabatically to a standard pressure of 1000 mb [Simpson, 1978]. The empirical formulation of Bolton [1980] is used here to estimate θ_e with an accuracy of 0.1°K in the tropics. Notice the higher θ_e values of 3°K to 10°K were observed over the LC/WCE compared to lower θ_e values over the CCE (inset in Figure 6b) similar to what was observed during EPIC [Raymond *et al.*,

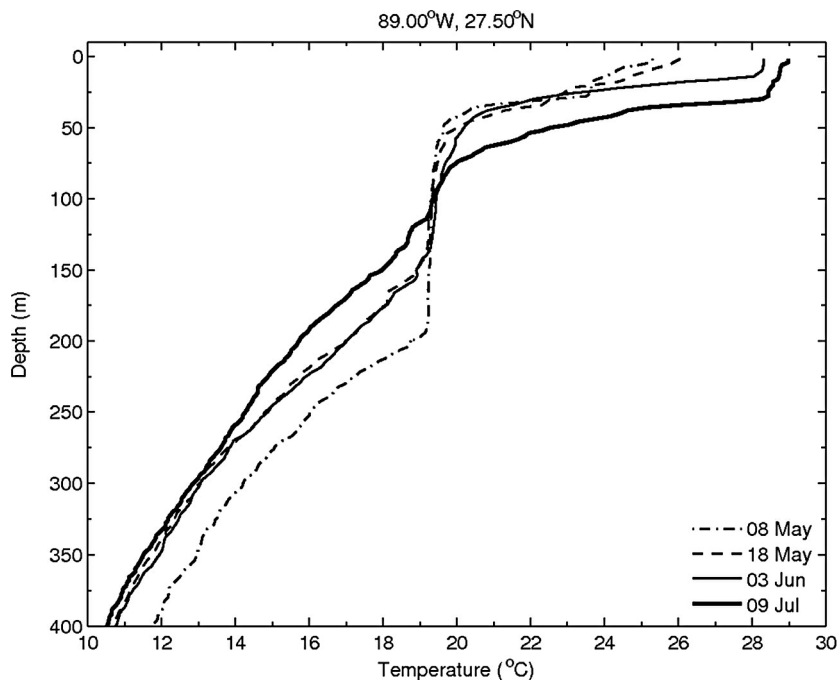


Figure 7. Evolution of temperature ($^\circ\text{C}$) at a point ($\sim 89.0^\circ\text{W}$, $\sim 27.5^\circ\text{N}$) located due south of the DwH, from airborne profilers. The profile for 8 May is from the first WP-3D flight (not shown in Figures 1 and 3).

2004]. This result points to the importance of elevated enthalpy fluxes over the warm ocean features [Hong *et al.*, 2000] where higher and more sustained fluxes occur compared to those over cooler ocean features [Shay *et al.*, 2000].

3.5. Subsurface Thermostat

One of the more salient aspects in the thermal structure near the DwH rig is the presence of a subsurface thermostat that

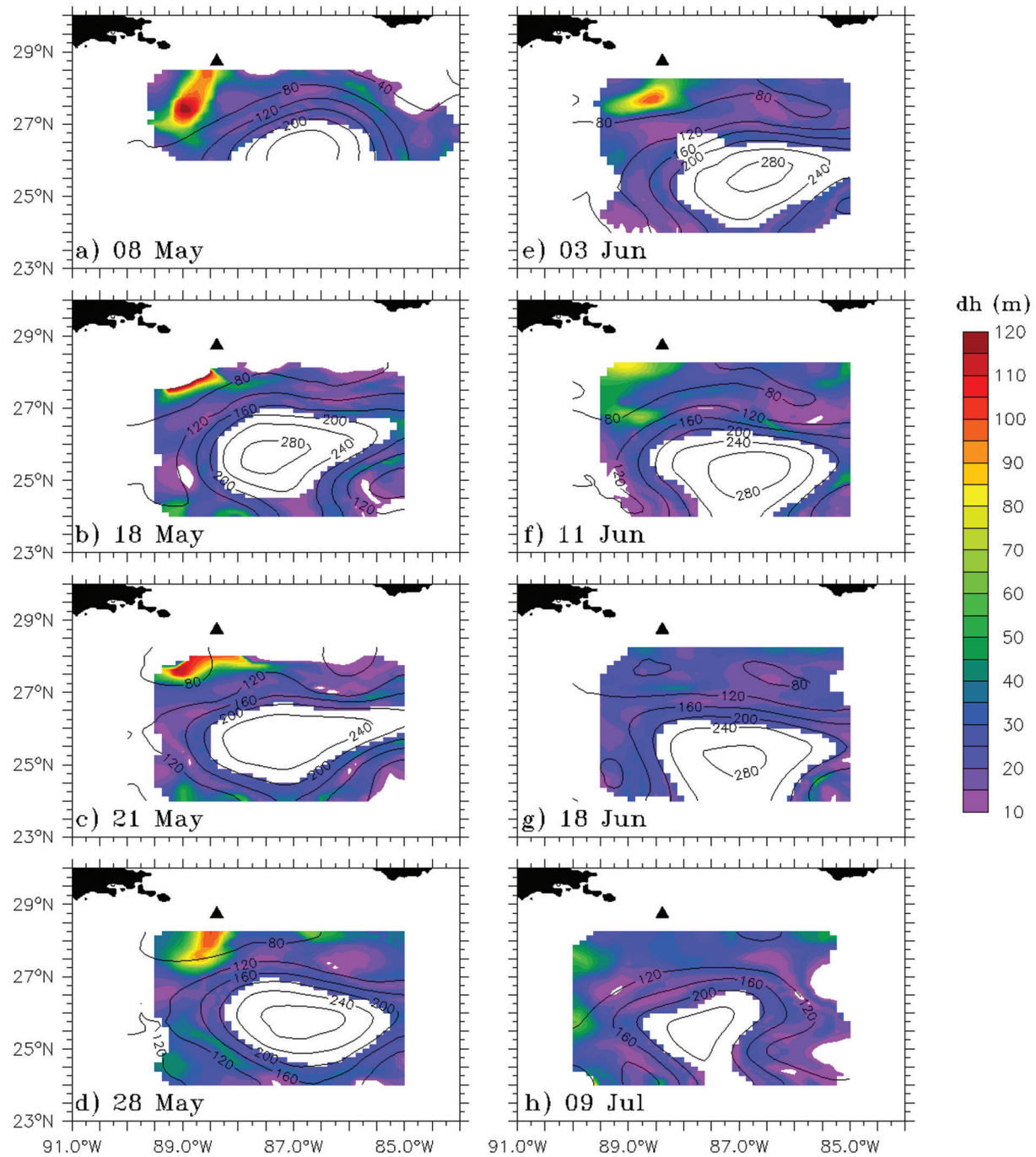


Figure 8. Thickness (dh) of the layer bounded by the 19°C and 20°C isotherms. Contours are for the depth of the 20°C isotherm (m). The bulge of the LC is blanked for presentation purposes.

extended between 30 and 200 m depths on 8 May. Homogeneous temperatures of $\sim 19^\circ\text{C}$ characterized this thick layer (Figure 7). Surface waters on top of this thermocline were strongly stratified, and temperatures decreased by nearly 7°C over the upper 50 m of the water column. By 18 May, this thermocline thickness was reduced by ~ 50 m and remained nearly constant until 3 June. By 9 July, the thermocline was nearly absent. Although this thermocline could be the remnant of a deep mixed layer potentially produced during winter by strong cold fronts [cf. Nowlin and McLellan, 1967], it is not clear that the evolution of this thermocline from 8 May to 9 July was driven solely by mixed layer dynamics, as temperatures below the 100 m depth level decreased with time. During mixed layer deepening events, SSTs decrease, whereas temperatures in the thermocline warm by the effect of vertical mixing induced by vertical current shears. In addition to mixed layer deepening events, these changes in thermal structure near the DwH rig were strongly influenced by the mesoscale and synoptic scale variability discussed above. In particular, the development of CCEs may explain the progressive cooling of waters below the 100 m depth level. Note that the temperature profile from 9 July was measured at the edge of a CCE (drop point 51, Figure 1h). The gradual warming of surface layer may have been caused by insolation, which is usually the case in the spring to summer transition period in the GoM.

Another striking aspect of the thermal structure near the DwH rig is the horizontal distribution of the thermocline. From 8 May to 11 June, the thickness (dh) of a nearly homogeneous water column, bounded by the 19°C and 20°C isotherms, shows consistent maximum values between 80 and 120 m south of the rig (Figure 8). The variability of the horizontal distribution of dh is constrained by the flow lines, represented here by the topography of H_{20} , which is a proxy for the main thermocline depth in the GoM [Shay *et al.*, 1998]. Intermediate levels of dh between 40 and 60 m originated at the regions of maximum dh and extended along the periphery of the LC, which suggests advection of these nearly homogeneous waters by the energetic background flows of more than 1 m s^{-1} .

A water mass analysis, based on AXCTDs deployed on 18 May, reveals the presence of unusual low salinity levels (< 36.2 psu) at two sampling points (53, 54) located at the

region of maximum dh (Figure 9a). These low salinity levels extended to the top of the thermocline, where temperatures ranged from 20°C to 28°C . These anomalous salinity levels do not correspond to water mass characteristics commonly observed in offshore stations over the LC, WCEs, CCEs, or Gulf Common Water. In the work of Nowlin and McLellan [1967], salinity levels between 32.5 and 36 psu were measured over the Louisiana-Texas continental shelf where maximum depths were less than 75 m presumably associated with Mississippi River outflow. Here the upper ocean low salinity levels were measured offshore. Over the surface layers occupied by these low salinity waters (upper 50 m depth), the buoyancy frequency represented anomalous peaks of about 16 and 18 cph at points 53 and 54, respectively, which is indicative of strong stratification (Figure 9b). Given that strong stratification reduces vertical mixing by turbulent process over the mixed layer base and the thermocline (e.g., Richardson numbers above criticality), diapycnal diffusion may have played a role in delineating these anomalous upper ocean salinity levels. At drop points 53 and 54, salinity levels decreased with temperature (or with depth) in waters warmer than 20°C (Figure 9a).

Without direct water samples, it is impossible to assert whether these low salinity levels were associated with fresh water from the Mississippi River runoff or with other substances diluted in the water column. However, the velocity field in the area of drop points 53 and 54 indicates that these water mass properties were transported in the southwest direction away from the DwH rig through the smaller-scale cyclone along the western edge of the LC (Figures 9c, d). The orientation of the velocity vector (vertically averaged over the upper 200 m in depth) is consistent with distributions of dh presented in Figures 8b and 9d.

3.6. Variability From Altimetry Products

The WP-3D data set not only provided a direct physical insight into important dynamical processes that occurred south of the DwH rig, it also provided an important time series of oceanographic parameters that can be used to calibrate altimetry products commonly used to forecast tropical cyclone intensity during the hurricane season [Mainelli *et al.*, 2008;

Figure 9. (opposite) Oceanographic conditions near the DwH during 18 May, from airborne probes. (a) Water mass from AXCTD profilers; STW, subtropical water; SAAIW, Sub-Antarctic intermediate water; GCW, Gulf Common Water; numbers indicate the drop point. (b) Buoyancy frequency (N: cph) from AXCTD profilers smoothed via polynomial fit. (c) Horizontal velocity from AXCP profiles; positive values for the velocity components u and v are (right) to the east and (up) to the north, respectively; the numbers on top of the profile indicate the drop point. (d) Snapshot of dh (as in Figure 7b) showing the location of the drop points presented in (a–c); the black triangle is the DwH; yellow diamonds are AXCTDs; red squares are AXCPs, and the black vectors originating in these squares represent horizontal currents depth-averaged over the upper 200 m.

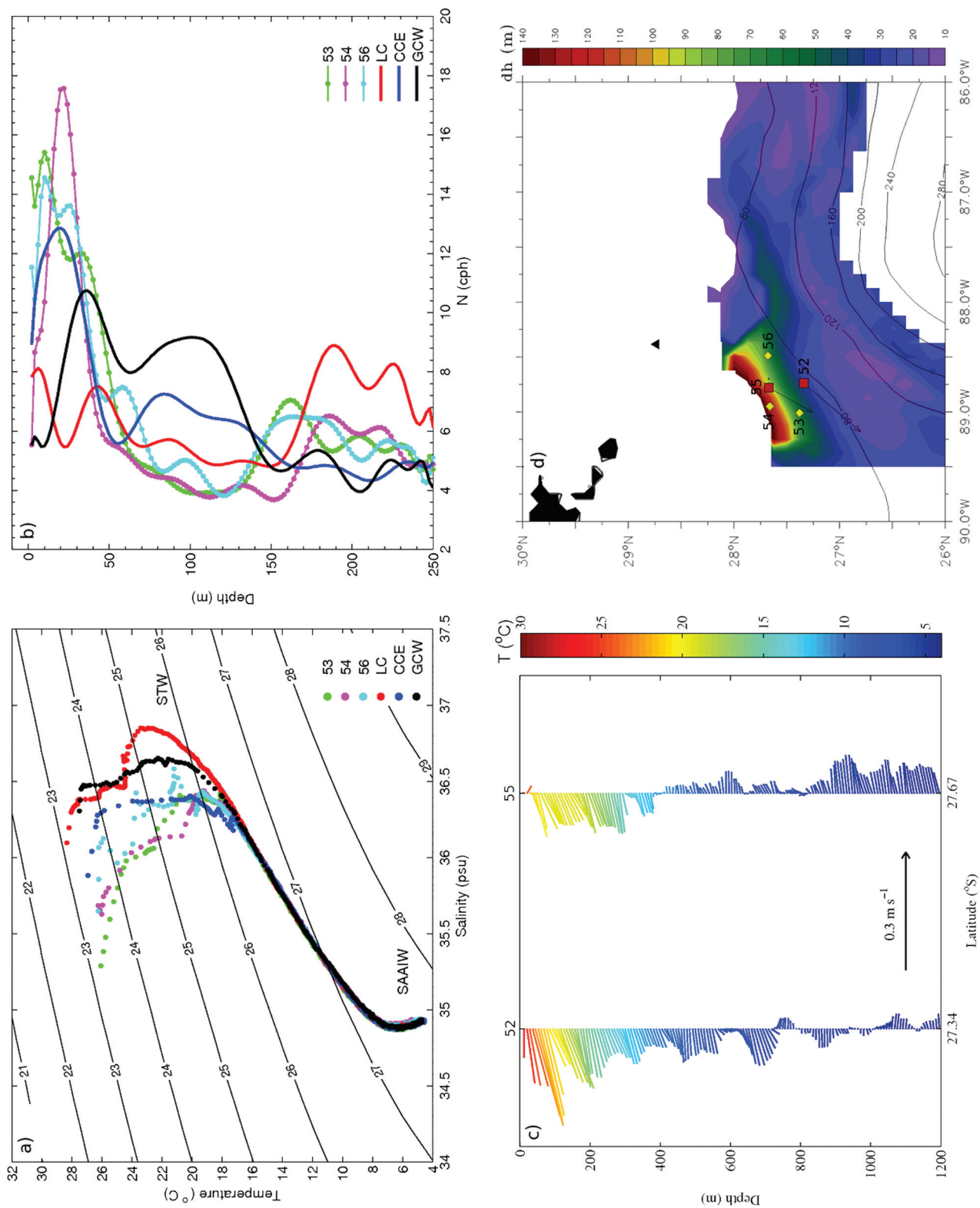


Figure 9

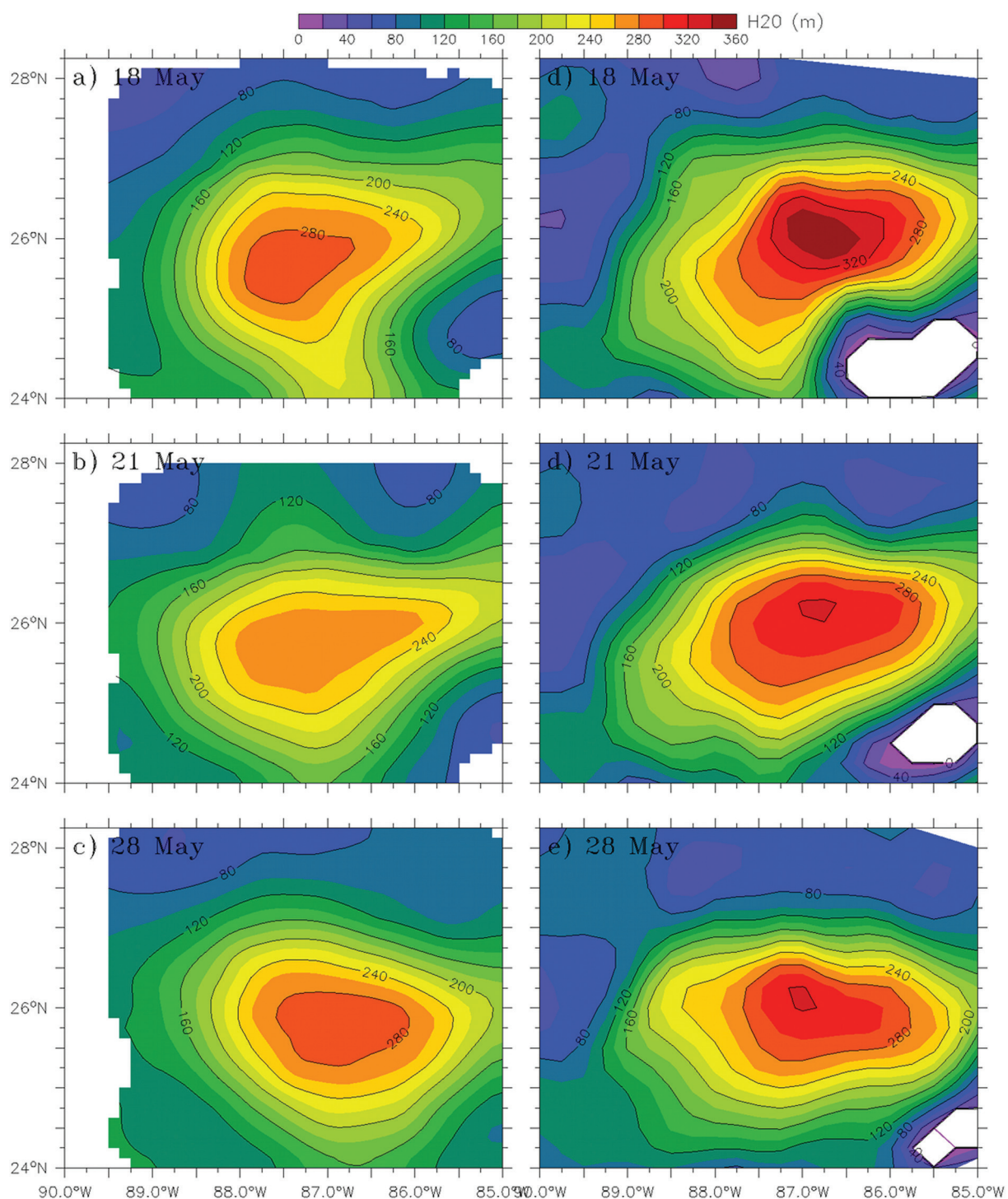


Figure 10. Comparison of in situ H_{20} (from airborne profilers, left panels) versus altimetry-based H_{20} (right panels). Altimetry-based H_{20} is derived from climatologic values of in situ H_{20} and sea surface height anomaly from NASA Jason-1 and Jason-2, and ESA Envisat altimeters, following a climatology cast within a two-layer model approach [Mainelli et al., 2008; Shay and Brewster, 2010]; Systematically Merged Atlantic Regional Temperature and Salinity climatology [Meyers, 2011] is used during this estimation of altimetry-based H_{20} variations.

Shay and Brewster, 2010]. One example is presented in Figure 10, where the comparison of in situ versus near real-time altimetry-based H_{20} shows a good agreement in the general aspects of the LC bulge and its evolution. Using the observed thermal structure, the Systematically Merged Atlantic Regional Temperature and Salinity climatology [Meyers, 2011] was used to estimate H_{20} from altimetry measurements cast within a two-layer model [Goni *et al.*, 1996]. The placement of the center of Franklin was within 15 to 20 km compared with in situ data (not shown). Moreover, the difference in H_{20} was within 20 m of the altimetry product. Calibrated altimetry products will help to investigate the LC variability during periods not covered by the WP-3D flights.

4. MODELS AND DATA ASSIMILATION

From a scientific perspective, profiler data were not only important in improving our understanding of the complex eddy shedding processes, but also provided an important source of additional near real-time, in situ observations for assimilation into operational ocean models that were used to estimate trajectories of oil transport. The model used is the HYbrid Coordinate Ocean Model (HYCOM; <http://www.hycom.org>). It is designed to use Lagrangian isopycnic coordinates throughout as much of the stratified ocean interior as possible, but dynamically transition to fixed vertical coordinates, either level (p) or terrain-following (σ), in regions where isopycnic coordinates are suboptimum [Bleck, 2002; Chassignet *et al.*, 2003; Halliwell, 2004]. The regional GoM HYCOM was run with horizontal resolution of 0.04° (~ 4 km) and 20 hybrid layers in the vertical. The lateral nested boundary conditions were generated from a multiyear, climatologically forced, 0.08° HYCOM Atlantic Ocean simulation.

4.1. Data Assimilation Approach

The data assimilation component of the nowcast/forecast system is the Navy Coupled Ocean Data Assimilation (NCODA) system, which was developed as an oceanographic version of the Multi-Variate Optimum Interpolation (MVOI) [Cummings, 2005] technique widely used in operational atmospheric forecasting. The latest version of NCODA implements a 3dvar solver as a replacement for the original MVOI technique. The 3dvar version is used in all HYCOM experiments described herein. NCODA assimilates both SSH anomalies from satellite altimetry on a track-by-track basis and SST. The impact of altimetry assimilation is tapered to zero toward the coast between the middle and upper regions of the continental slope. Surface observations of SSH and SST observations are projected vertically downward using the Modular Ocean Data Assim-

ilation System (MODAS) [Fox *et al.*, 2002]. MODAS is a statistical technique based on a regression analysis between SSH anomalies and SST observations and historical subsurface temperature and salinity profiles. These synthetic profiles are only calculated along the altimeter tracks and are used to adjust the interior water mass properties (temperature and salinity) using increments based on the previous day's forecast.

4.2. Twin Numerical Experiments

In addition to transmitting data via the Global Telecommunication System (GTS) for assimilation into the GoM HYCOM in real-time via the NCODA system to improve the simulations at the Naval Oceanographic Office for trajectory analyses where an observation window of ± 36 h for altimetry and ± 12 h for other observations was used for each daily update, the impact of the aircraft measurements on forecast accuracy is assessed using twin numerical experiments in delayed reanalysis mode. The same observational time windows are used in the daily updates, except all observations are available without delay. This enables the update cycle to be initialized from the previous-day analysis instead of from the 4 day old analysis. The first experiment assimilated all observations including the airborne surveys, while the second experiment is identical except for denying the airborne observations. The HYCOM experiment that assimilated WP-3D data in the GoM domain (hereafter assimilative P3-GoM-HYCOM) reproduced H_{20} values that, in general, were lower than in situ H_{20} values; the overall bias for the nine flights was ~ 2 m (Table 2). The experiment that denied WP-3D data (hereafter GoM-HYCOM) also underestimated H_{20} levels with an overall bias of -3 m; that is, nearly twice as large as the bias from P3-GoM-HYCOM. However, a scatter plot comparing in situ versus model H_{20} values presents a nonlinear relationship, suggesting a grouping in three clusters defined in terms of in situ H_{20} : (i) $H_{20} \leq 100$ m, (ii) $100\text{m} < H_{20} \leq 200\text{m}$, and (iii) $H_{20} > 200\text{m}$ (Figure 11a).

Table 2. Statistical Parameters of the Comparison of In Situ Versus Model H_{20} , From Data Presented in Figure 10

	Cluster 1		Cluster 2		Cluster 3	
	$H_{20} \leq 100$ m		$100\text{ m} < H_{20} \leq 200\text{ m}$		$H_{20} > 200\text{ m}$	
	Slope	Bias (m)	Slope	Bias (m)	Slope	Bias (m)
DA ^a	0.63	8.0	0.72	-4.0	1.13	-16.0
No-DA ^a	0.53	11.6	0.60	-6.2	1.11	-22.0

^aDA and No-DA stand for model outputs with and without assimilation of WP-3D data, respectively.

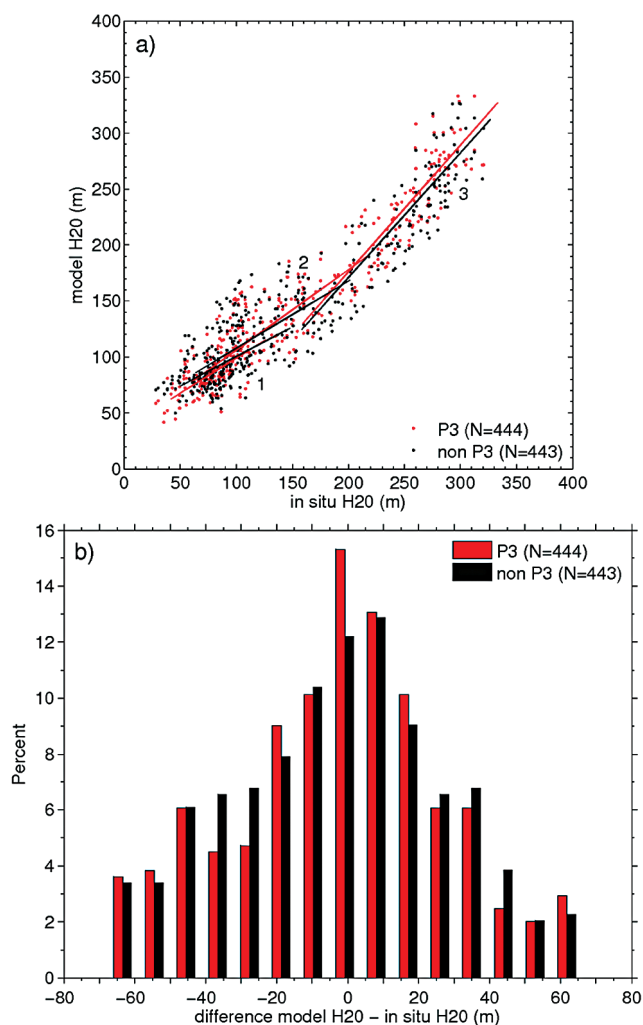


Figure 11. (a) Comparison of in situ versus model H_{20} for the nine flights and for model data whose individual difference respect to in situ data is less than three standard deviations (94.5% and 94.3% of all data for DA and No-DA, respectively); DA and No-DA stand for model outputs with and without assimilation of WP-3D data, respectively; the numbers 1, 2, and 3 are indices for clusters of data where in situ H_{20} satisfies, respectively, the following conditions: $H_{20} \leq 100$ m, $100 \text{ m} < H_{20} \leq 200$ m, and $H_{20} > 200$ m (slope and bias of these data clusters are presented in Table 2). (b) Histogram of differences for data in (a); the bin size is 15.

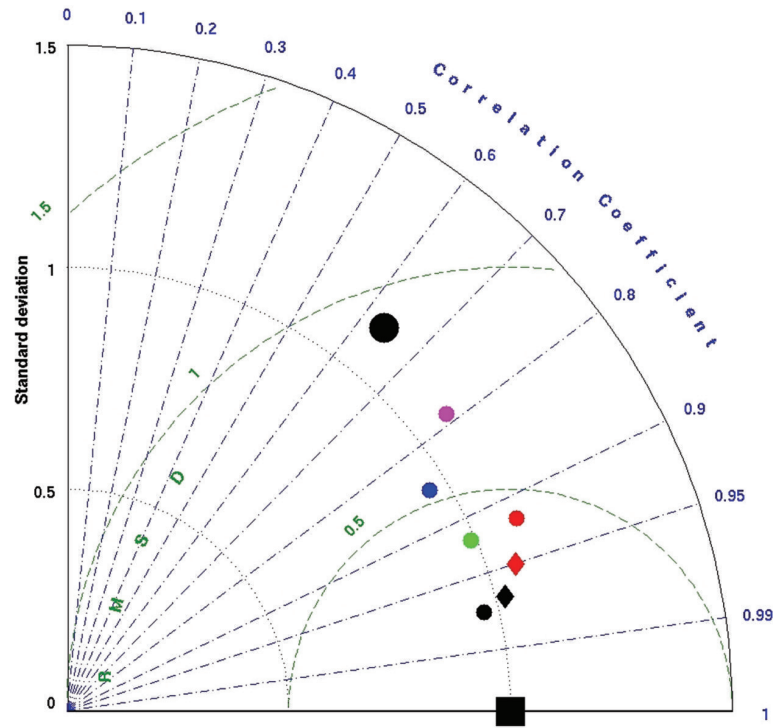
These clusters represent cold features, GCW, and warm features, respectively. Individual analysis over these clusters indicate that, in the case of P3-GoM-HYCOM, H_{20} is overestimated by an average of 8 m in cold features and underestimated by an average of 4 and 16 m in GCW and warm features, respectively. This tendency is similar in the GoM-HYCOM experiment, where H_{20} is overestimated by ~ 12 m in cold features and underestimated by 6 and 22 m in GCW and warm features, respectively. That is, the assimilation of WP-3D data improved the representation of H_{20} in P3-GoM-HYCOM between 28% and 34%, compared to GoM-HYCOM. As suggested in Figure 11b, approximately 43% and 48% of model H_{20} values presented a difference of more than 20 m with respect to in situ data in the P3-GoM-HYCOM and GoM-HYCOM experiments, respectively.

4.3. Analysis of Products

Errors in these two analysis products are quantified in comparison to the profiler observations to determine the error reduction resulting from assimilation of the aircraft profiles. The value of the aircraft observations for evaluating ocean model analyses is approached by comparing several different ocean model analyses to the observations. To simplify these comparisons, *Taylor* [2001] diagrams (Figure 12) are constructed by first removing the overall mean from each field, normalizing each field by the variance of the observed field, and then calculating the three different but related metrics represented on this diagram (correlation coefficient, RMS amplitude, and RMS error). Errors are analyzed for two fields over all 9 flight days: temperature between depths of 30 and 360 m from the aircraft and model profiles sampled at the same locations and horizontal maps of H_{20} calculated from these model and observed profiles (Figure 12). To provide a reference point to assess analysis improvements resulting from data assimilation, a nonassimilative HYCOM experiment was also compared to observations, with the large black circles in the Taylor diagrams demonstrating the poor comparison between this numerical experiment and observations. Comparisons between seven data-assimilative ocean analyses and observations demonstrate that substantial error reductions

Figure 12. (opposite) *Taylor* [2001] diagrams of (a) temperature ($^{\circ}\text{C}$) between 30 and 360 m depth and (b) H_{20} (m) comparing several model analyses to the observed fields. A perfect comparison is marked by the large black square. The quality of each analysis field is inversely proportional to the distance from this reference point. The large black circle represents a nonassimilative Gulf of Mexico Hybrid Coordinate Ocean Model (HYCOM) run. Black and red diamonds compare the P3-GoM-HYCOM and GoM-HYCOM experiments performed at NRL for the Observing System Experiment. Analyses from several other models are included for comparison. The only two models that assimilated aircraft observations are P3-GoM-HYCOM (black diamond) and global HYCOM (small black circle).

T, 30-360m (all 9 flights)



Reference Points

- Perfect comparison
- No assimilation (GoM HYCOM)

P-3 Impact Analysis

- ◆ GoM HYCOM (includes P-3)
- ◆ GoM HYCOM (denies P-3)

Other Data-Assimilative Analyses

- Navy Global HYCOM
- NRL IASNFS NCOM
- NCSU SABGOM ROMS
- NOAA/NOS NGOM POM
- NOAA/NCEP/EMC RTOFS HYCOM

H₂₀ (all 9 flights)

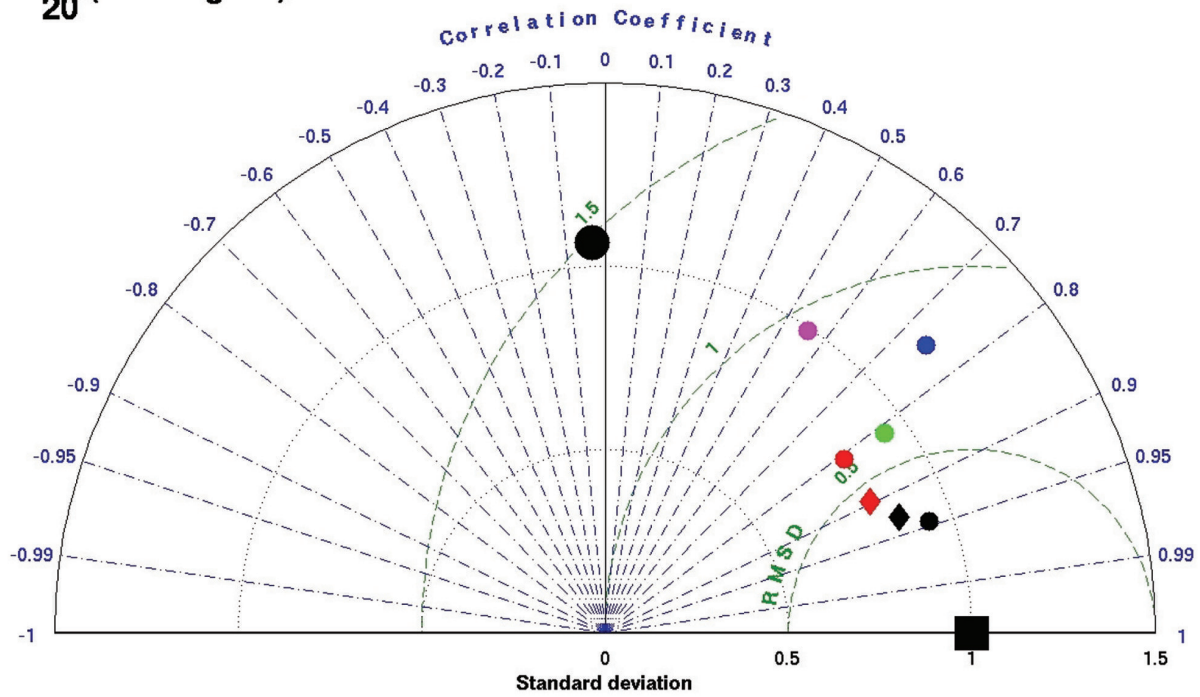


Figure 12

result from assimilation of these observations, although the levels of error reduction varies among models. The model with the least error reduction (RTOFS-HYCOM) [Mehra and Rivlin, 2008] is known to have a problem with their version of the model that will be fixed during the next upgrade of the operational system (H. Tolman, personal communication, 2011). Four models with intermediate error reduction (South Atlantic Bight Gulf of Mexico-Regional Ocean Model System, <http://omgrhe.meas.ncsu.edu/Group/>; Intra-Americas Sea Nowcast-Forecast System Navy Coastal Ocean Model [Ko *et al.*, 2008]; National Oceanographic and Atmospheric Administration/National Ocean Service Gulf of Mexico Model, <http://www.nauticalcharts.noaa.gov/csdl/NGOM.html>; and experiment GoM-HYCOM run for the Observing System Experiment (OSE)) did not assimilate the aircraft profiles. The two models that assimilated profiles observations (global HYCOM [Chassignet *et al.*, 2007] and experiment P3-GoM-HYCOM) produced the analyses that resulted in the largest error reduction compared to the non-assimilative models, demonstrating the positive impact of assimilating the aircraft observations.

The reduction in bias and RMS error on each of the nine flight days resulting from assimilation of the aircraft observations is illustrated by comparing temperature between 30 and 360 m between experiments P3-GoM-HYCOM and GoM-HYCOM (Figure 13). The reduction in temperature

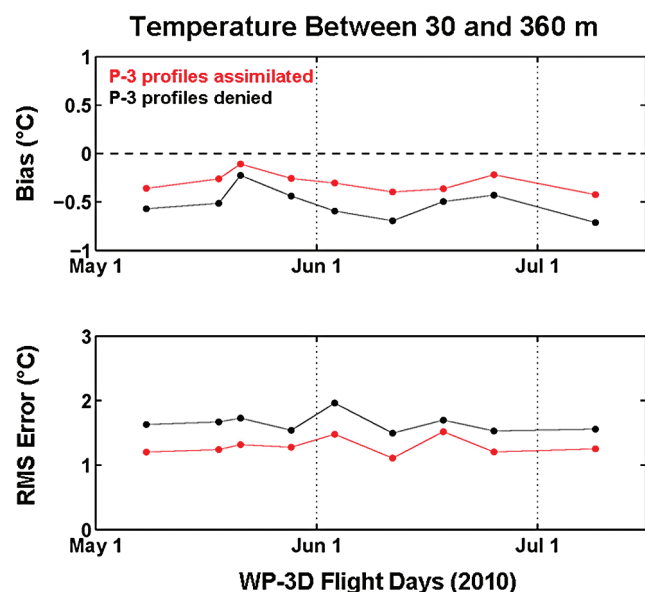


Figure 13. (top) Mean bias ($^{\circ}\text{C}$) and (bottom) RMS error ($^{\circ}\text{C}$) for temperature between 30 and 360 m. The black (red) curves represent model experiments with GoM-HYCOM where P-3 observations were denied (accepted).

bias (not measured by the Taylor diagrams) is about 50% on average, while the reduction of average RMS error is 25% to 30%, demonstrating a positive impact of aircraft data assimilation. These results are considered an initial assessment of this impact because it depends on factors such as the ocean model, data assimilation method, and details of the assimilation cycle such as the observation time windows and whether it is performed in real-time versus delayed reanalysis mode. Further studies must consider these factors and employ observations that were not assimilated but unavailable for the present study to determine if the present results are robust and to confidently quantify the impact of aircraft data assimilation.

5. SUMMARY

The aircraft ocean observations provided a comprehensive data set to study the GoM ocean current system during a bulging of the LC and subsequent eddy-shedding event [Leben, 2005; Vukovich, 2007; Hamilton *et al.*, this volume]. This data set provided additional observations that were assimilated in real-time into Navy HYCOM analyses that were used with other models to forecast oil trajectories and will provide valuable information for retrospective studies of the DwH oil spill. Despite a hurricane season that did not see any significant land-falling storms along the northern GoM coast [Jaimes and Shay, 2009; Halliwell *et al.*, 2011], the data set acquired will also help study the 3-D, spatially evolving ocean system that will impact forecasting hurricane intensity changes in subsequent seasons.

Experimental objectives were to provide synoptic data over a large scale to measure the possible shedding of a Franklin from the LC and provide oceanic structural data for predictive ocean models at the Naval Oceanographic Office for potential pathways of the oil [Liu *et al.*, this volume; Walker *et al.*, this volume]. Despite some initial problems with the AXCPs that were resolved during the experiment, the thermal structure was well resolved from the aircraft measurements within measurement uncertainty. As in a hurricane, the aircraft allows us to survey a regional area (in this case on the scale of the LC) over about 8 to 10 h. The importance of such aircraft measurements cannot be overstated in that ocean models with assimilation systems require these data where the constraint is the data assimilation cycle. Whether in real-time or delayed reanalysis mode, each daily update is performed using observations within a narrow window (± 36 h for altimetry and ± 12 h for other observations). The aircraft observations permit the synoptic structure of the LC region to be resolved within this observation window. By contrast, at least several days are required to obtain synoptic coverage from altimetry and days to weeks to

obtain similar synoptic coverage from a ship or glider. Given the narrow ± 12 h observation window, aliasing of earlier observations is avoided, but only a small fraction of the profiles collected from a ship or glider will be assimilated during each daily analysis update. Thus, careful attention needs to be afforded to understanding how the update cycle affects the impact of these differing data sets. Twin OSE experiments used to evaluate the impact of aircraft data assimilation were conducted in delayed reanalysis mode representing the unrealistic situation where all observations are instantaneously made available to the GTS. The impact of delayed observations on real-time ocean analyses must be considered in future studies, while methods to post quality-controlled aircraft observations on the GTS more rapidly must be explored. Even with the broad-scale aircraft measurements at 7 to 10-day intervals, the approach did not resolve the rapidly evolving smaller-scale structures along the periphery of the LC. Such sampling and aliasing issues need to be carefully looked at in subsequent studies by combining all data sets including the evolution of the feature at the BOEMRE moorings deployed as part of the LC Dynamics Study.

These measurements provide important data to correlate to satellite measurements and numerical model simulations. Of particular interest, it is an opportunity to compare synthetic to in situ temperature profiles to assess the robustness of these satellite-derived profiles. From a scientific perspective, these data are useful in improving our understanding of the complex eddy shedding processes associated with Eddy Franklin. Through a series of detachments and reattachments, this data set represents an opportunity to evaluate HYCOM performance under light wind conditions. These measurements are also of equal importance for the hurricane season to calibrate radar altimeter-derived oceanic heat content variability used in intensity forecast models [DeMaria *et al.*, 2005; Mainelli *et al.*, 2008].

Acknowledgments. The research team gratefully acknowledges support from the NOAA Oil Spill Grant from Office of Response and Restoration (Dr. Debbie Payton) and Office of Oceanic and Atmospheric Research (Ms. Judy Gray) through NOAA's *Cooperative Institute for Marine and Atmospheric Studies (CIMAS)* directed by Dr. Peter Ortner at the University of Miami. We also would like to acknowledge Drs. Alexis Lugo-Fernandez and Ronald Lai of the Department of the Interior's Bureau of Ocean Energy Management, Regulation and Enforcement (BOEMRE) Dynamics of the Loop Current Study (BOEMRE Contract M08PC20052). The authors are grateful to the pilots, engineers, and technicians at NOAA's Aircraft Operation Center (Captain Brad Kearse, Dr. Jim McFadden, and Mr. Steven Paul) for conducting these missions that allowed the community to be out in front of the DwH spill. We also thank Dr. Robert Atlas (Director of NOAA AOML), Dr.

Molly Baringer (PhOD) and Dr. Rob Rodgers (HRD) who made these missions possible during DwH and hurricane missions through the Hurricane Forecast Improvement Project (HFIP) and the Intensity Forecast Experiment (IFEX). The collaborative ties with Environmental Modeling Center directed by Dr. Hendrick Tolman at the National Center for Environmental Protection is also greatly appreciated. We thank the institutions and researchers who provided temperature profiles from numerical models to generate Figure 13: Dr. Dong-Shan Ko, NRL-Stennis (IASNFS-NCOM); Dr. Ruoying He, North Carolina State University (SABGOM-ROMS); Dr. Richard Patchen, NOAA/NOS (NGOM-POM). The NOAA/NCEP/EMC RTOFS-HYCOM and Navy global HYCOM analyses were obtained from public servers. Rio05 was produced by CLS Space Oceanography Division. Finally, we thank the reviewers for their insights and commentary that improved the manuscript.

REFERENCES

- Bleck, R. (2002), An oceanic general circulation framed in hybrid isopycnic-Cartesian coordinates, *Ocean Modell.*, *4*, 55–88.
- Bolton, D. (1980), The computation of equivalent potential temperature, *Mon. Weather Rev.*, *108*, 1046–1053.
- Boyd, J. (1987), Improved depth and temperature conversion equations for Sippican AXBTs, *J. Atmos. Oceanic Technol.*, *4*, 545–551.
- Chassignet, E. P., L. Smith, G. R. Halliwell Jr., and R. Bleck (2003) North Atlantic simulation with the hybrid coordinate ocean model (HYCOM): Impact of the vertical coordinate choice and resolution, reference density, and thermobaricity, *J. Phys. Oceanogr.*, *33*, 2504–2526.
- Chassignet, E. P., H. E. Hurlburt, O. M. Smedstad, G. R. Halliwell, P. J. Hogan, A. J. Wallcraft, and R. Bleck (2007), Ocean Prediction with the HYbrid Coordinate Ocean Model (HYCOM), *J. Mar. Syst.*, *65*, 60–83.
- Chérubin, L. M., W. Sturges, and E. P. Chassignet (2005), Deep flow variability in the vicinity of the Yucatan Straits from a high-resolution numerical simulation, *J. Geophys. Res.*, *110*, C04009, doi:10.1029/2004JC002280.
- Chérubin, L. M., Y. Morel, and E. P. Chassignet (2006), Loop Current ring shedding: The formation of cyclones and the effect of topography, *J. Phys. Oceanogr.*, *36*, 569–591.
- Cummings, J. A. (2005), Operational multivariate ocean data assimilation, *Q. J. R. Meteorol. Soc.*, *131*, 3583–3604.
- DeMaria, M., M. Mainelli, L. K. Shay, J. A. Knaff, and J. Kaplan (2005), Further improvements to the statistical hurricane intensity prediction scheme (SHIPS), *Weather Forecasting*, *20*, 531–543.
- Elliot, B. A. (1982), Anticyclonic rings in the Gulf of Mexico, *J. Phys. Oceanogr.*, *12*, 1292–1309.
- Fox, D. N., C. N. Barron, M. R. Carnes, M. Booda, G. Peggion, and J. Van Gurley (2002), The modular ocean data assimilation system, *Oceanography*, *15*, 22–28.
- Goni, G. J., S. Kamholz, S. L. Garzoli, and D. B. Olson (1996), Dynamics of the Brazil/Malvinas confluence based on inverted

- echo sounders and altimetry, *J. Geophys. Res.*, *95*, 22,103–22,120.
- Halliwel, G. R., Jr. (2004), Evaluation of vertical coordinate and vertical mixing algorithms in the hybrid-coordinate ocean model (HYCOM), *Ocean Modell.*, *7*, 285–322.
- Halliwel, G. R., Jr., L. K. Shay, J. K. Brewster, and W. J. Teague (2011), Evaluation and sensitivity analysis to an ocean model to hurricane Ivan, *Mon. Weather Rev.*, *139*(3), 921–945.
- Hamilton, P. (1992), Lower continental slope cyclonic eddies in the central Gulf of Mexico, *J. Geophys. Res.*, *97*, 2185–2200.
- Hamilton, P., K. A. Donohue, R. R. Leben, A. Lugo-Fernández, and R. E. Green (2011), Loop Current observations during spring and summer of 2010: Description and historical perspective, in *Monitoring and Modeling the Deepwater Horizon Oil Spill: A Record-Breaking Enterprise*, *Geophys. Monogr. Ser.*, doi:10.1029/2011GM001116, this volume.
- Hock, T. J., and J. L. Franklin (1999), The NCAR GPS dropwindsonde, *Bull. Am. Meteorol. Soc.*, *80*, 407–420.
- Hong, X., S. W. Chang, S. Raman, L. K. Shay, and R. Hodur (2000), The interaction between Hurricane Opal (1995) and a warm core eddy in the Gulf of Mexico, *Mon. Weather Rev.*, *128*, 1347–1365.
- Jaimes, B., and L. K. Shay (2009), Mixed layer cooling in meso-scale oceanic eddies during hurricanes Katrina and Rita, *Mon. Weather Rev.*, *137*, 4188–4207.
- Johnson, G. C. (1995), Revised XCTD fall-rate equation coefficients from CTD data, *J. Atmos. Oceanic Technol.*, *12*, 1367–1373.
- Ko, D. S., P. J. Martin, C. D. Rowley, and R. H. Preller (2008), A real-time coastal ocean prediction experiment for MREA04, *J. Mar. Syst.*, *69*, 17–28, doi:10.1016/j.jmarsys.2007.02.022.
- Kunze, E. (1985), Near-inertial wave propagation in geostrophic shear, *J. Phys. Oceanogr.*, *15*, 544–565.
- Leben, R. R. (2005), Altimeter-derived Loop Current metrics, in *Circulation in the Gulf of Mexico: Observations and Models*, *Geophys. Monogr. Ser.*, vol. 161, edited by W. Sturges and A. Lugo-Fernandez, pp. 181–201, AGU, Washington, D. C.
- Liu, Y., R. H. Weisberg, C. Hu, C. Kovach, and R. Riethmüller (2011), Evolution of the Loop Current system during the *Deepwater Horizon* oil spill event as observed with drifters and satellites, in *Monitoring and Modeling the Deepwater Horizon Oil Spill: A Record-Breaking Enterprise*, *Geophys. Monogr. Ser.*, doi:10.1029/2011GM001127, this volume.
- Mainelli, M., M. DeMaria, L. K. Shay, and G. Goni (2008), Application of oceanic heat content estimation to operational forecasting of recent category 5 hurricanes, *Weather Forecasting*, *23*, 3–16.
- Mehra, A., and I. Rivlin (2008), A real time ocean forecast system for the North Atlantic, *Terr. Atmos. Ocean. Sci.*, *21*, 211–228.
- Meyers, P. C. (2011), Development and analysis of the Systematically Merged Atlantic Regional Temperature and Salinity (SMARTS) climatology for satellite-derived ocean thermal structure, M.S. thesis, 99 pp., Univ. of Miami, Coral Gables, Fla.
- Mooers, C. N. K., and G. Maul (1998), Intra-Americas sea circulation, in *The Sea*, vol. 11, *The Global Coastal Ocean, Regional Studies and Syntheses*, edited by A. Robinson and K. H. Brink, pp. 183–208, John Wiley, New York.
- Nof, D. (2005), The momentum imbalance paradox revisited, *J. Phys. Oceanogr.*, *35*, 1928–1939.
- Nowlin, W. D., Jr., and H. J. McLellan (1967), A characterization of the Gulf of Mexico waters in winter, *J. Mar. Res.*, *25*, 29–59.
- Nowlin, W. D., Jr., and J. M. Hubertz (1972), Contrasting summer circulation patterns for the eastern Gulf, in *Contributions on the Physical Oceanography of the Gulf of Mexico, Texas A&M Oceanogr. Ser.*, vol. 2, edited by L. R. A. Capurro and J. L. Reid, pp. 119–138, Gulf, Houston, Tex.
- Raymond, D. J., S. K. Esbensen, C. Paulson, M. Gregg, C. Bretherton, W. A. Peterson, R. Cifelli, L. Shay, C. Ohlmann, and P. Zuidema, (2004), EPIC2001 and the coupled ocean-atmosphere system of the tropical East Pacific, *Bull. Am. Meteorol. Soc.*, *85*, 1341–1354.
- Rio, M.-H., and F. Hernandez (2004), A mean dynamic topography computed over the world ocean from altimetry, in situ measurements, and a geoid model, *J. Geophys. Res.*, *109*, C12032, doi:10.1029/2003JC002226.
- Rogers, R., et al. (2006), The intensity forecasting experiment (IFEX), a NOAA multiple year field program for improving intensity forecasts, *Bull. Am. Meteorol. Soc.*, *87*, 1523–1537.
- Sanford, T. B., R. G. Drever, J. H. Dunlap, and E. A. D’Asaro (1982), Design, operation and performance of an expendable temperature and velocity profiler (XTVP), *Rep. APL-UW 8110*, 83 pp., Appl. Phys. Lab., Univ. of Washington, Seattle.
- Sanford, T. B., P. G. Black, J. Haustein, J. W. Feeney, G. Z. Forristall, and J. F. Price (1987), Ocean response to a hurricane. Part I: Observations, *J. Phys. Oceanogr.*, *17*, 2065–2083.
- Scharroo, R., W. H. F. Smith, and J. L. Lillibridge (2005), Satellite altimetry and the intensification of Hurricane Katrina, *Eos Trans. AGU*, *86*(40), 366, doi:10.1029/2005EO400004.
- Schmitz, W. J., Jr. (2005), Cyclones and westward propagation in the shedding of anticyclonic rings from the Loop Current, in *Circulation in the Gulf of Mexico: Observations and Models*, *Geophys. Monogr. Ser.*, vol. 161, edited by W. Sturges and A. Lugo-Fernandez, pp. 241–261, AGU, Washington, D. C.
- Shay, L. K., and J. K. Brewster (2010), Eastern Pacific oceanic heat content estimation for hurricane intensity forecasting, *Mon. Weather Rev.*, *138*, 2110–2131.
- Shay, L. K., and E. W. Uhlhorn (2008), Loop Current response to hurricanes Isidore and Lili, *Mon. Weather Rev.*, *137*, 3248–3274.
- Shay, L. K., A. J. Mariano, S. D. Jacob, and E. H. Ryan (1998), Mean and near-inertial response to hurricane Gilbert, *J. Phys. Oceanogr.*, *28*, 858–889.
- Shay, L. K., G. J. Goni, and P. G. Black (2000), Effects of a warm oceanic feature on Hurricane Opal, *Mon. Weather Rev.*, *128*, 1366–1383.
- Simpson, R. H. (1978), On the computation of equivalent potential temperature, *Mon. Weather Rev.*, *106*, 124–130.
- Sturges, W., and R. Leben (2000), Frequency of ring separations from the Loop Current in the Gulf of Mexico: A revised estimate, *J. Phys. Oceanogr.*, *30*, 1814–1819.
- Taylor, K. E. (2001), Summarizing multiple aspects of model performance in a single diagram, *J. Geophys. Res.*, *106*, 7183–7192.

- Uhlhorn, E. W., P. G. Black, J. L. Franklin, M. Goodberlet, J. Carswell, and A. S. Goldstein (2007), Hurricane surface wind measurements from an operational stepped frequency microwave radiometer, *Mon. Weather Rev.*, *135*, 3070–3085.
- Vukovich, F. M. (2007), Climatology of ocean features in the Gulf of Mexico using satellite remote sensing data, *J. Phys. Oceanogr.*, *37*, 689–707.
- Walker, N. D., et al. (2011), Impacts of Loop Current frontal cyclonic eddies and wind forcing on the 2010 Gulf of Mexico oil spill, in *Monitoring and Modeling the Deepwater Horizon Oil Spill: A Record-Breaking Enterprise*, *Geophys. Monogr. Ser.*, doi:10.1029/2011GM001120, this volume.
- Zavala-Hidalgo, J., S. L. Morey, and J. J. O'Brien (2003), Cyclonic eddies northeast of the Campeche Bank from altimetry data, *J. Phys. Oceanogr.*, *33*, 623–629.
- J. K. Brewster, B. Jaimes, E. C. McCaskill, P. Meyers, and L. K. Shay, Rosenstiel School of Marine and Atmospheric Science, Division of Meteorology and Physical Oceanography, University of Miami, 4600 Rickenbacker Causeway, Miami, FL 33149, USA. (nshay@rsmas.miami.edu)
- G. R. Halliwell Jr., NOAA Atlantic Oceanographic and Meteorological Laboratory, Physical Oceanography Division, 4301 Rickenbacker Causeway, Miami, FL 33149, USA.
- P. Hogan, Naval Research Laboratory, Stennis Space Center, MS 39529, USA.
- F. Marks and E. Uhlhorn, NOAA Atlantic Oceanographic and Meteorological Laboratory, Hurricane Research Division, 4301 Rickenbacker Causeway, Miami, FL 33149, USA.
- O. M. Smedstad, QinetiQ North America, Stennis Space Center, MS 39529, USA.

